ARTICLES
https://doi.org/10.1038/s41929-019-0332-5

nature catalysis

Selecting between two transition states by which water oxidation intermediates decay on an oxide surface

Xihan Chen[1], Daniel J. Aschaffenburg[1] and Tanja Cuk[1,2,3*]

Although catalytic mechanisms on electrode surfaces have been proposed for decades, the pathways by which the product's chemical bonds evolve from the initial charge-trapping intermediates have not been resolved. Here, we discover a reactive intermediate population with states in the middle of a semiconductor's bandgap that reveal the dynamics of two parallel transition state pathways for their decay. After phototriggering the water oxidation reaction from the *n*-$SrTiO_3$ surface, the microsecond decay of the intermediates affirms transition state theory through two distinct time constants, the primary kinetic salt and H/D kinetic isotope effects, realistic activation barrier heights and transition state theory pre-factors. Furthermore, we show that the reaction conditions can be adjusted to allow selection between the two pathways, one characterized by a labile intermediate facing the electrolyte (the oxyl), and the other by a lattice oxygen (the bridge). In summary, we experimentally isolate an important activation barrier in multi-electron transfer water oxidation and, in doing so, identify competing mechanisms for O_2 evolution at surfaces.

Electrochemical reactions are important for transforming electrical energy into chemical energy and the most complex multistep reactions are thought to occur at electrode surfaces[1,2]. The surface plays the role of a catalyst, reconfiguring reactants into products through a series of electron-transfer and chemical bond-making and breaking events[2,3]. The mechanistic pathways by which these events occur differentiate the catalysts and have been advocated by decades of electrochemical investigations that track product evolution[4–6]. However, important questions remain unresolved, such as how to select between faster and slower pathways[7,8], and the nature of transition states in relation to critical reaction steps[5,9], including the formation of the product's chemical bonds[10,11]. More generally, the properties of electrochemically controlled catalysis at an electrode surface (for example, efficient funnelling of charge to catalytic events and the existence of multiple and tuneable pathways) have yet to be explained by the dynamics that connects the intermediate steps to product evolution.

Multi-electron transfer water oxidation is a canonical electrochemical reaction that can occur efficiently both at an electrode[12] and in a homogenous form[13], and for which there have been a number of mechanistic studies on the intermediate steps. In photosystem II, the oxygen-evolving complex (OEC)[14] receives charge from the photoinduced charge separation that occurs in the chromophore antenna[15], and the configuration of the OEC after each charge transfer has been investigated by mid-infrared[16], optical[17] and X-ray studies[14,15,18]. Despite such thorough investigations of the homogeneous OEC, the reaction intermediates that trap charge, and should initiate O–O bond formation, have been directly observed only at the heterogeneous transition metal oxide surface. The reaction intermediates that are generated following the first electron transfer (one-electron intermediates) have been revealed in forms such as Ti–O$^\bullet$, Fe(ɪv)=O and Co(ɪv)=O (refs. [19–21]). In time-resolved studies, photoexcitation is used, restricting the potential at which holes initiate the oxidation reaction to the electronic levels in the photosensitizer (for example, a dye molecule or semiconductor). On the other hand, once charge trapping has occurred, the subsequent steps should at least be analogous to fully electrochemical systems driven below the potential of surface-trapped charge, and the intermediates should similarly appear as Ti–O$^\bullet$, Fe(ɪv)=O or Co(ɪv)=O. By contrast to homogeneous catalysts such as the OEC (where only one or two one-electron intermediates should occur in a cycle) in heterogenous catalysts they are expected to considerably populate a surface, which explains why they have been uniquely observed in heterogeneous systems and also supports heterogeneous mechanisms that involve many interconnected sites[22,23].

The dynamics of how these intermediates decay and then proceed to the next event in the cycle, presumed to be the formation of the single O–O bond, has not yet been revealed through distinct activation barriers or their associated transition states. The difficulty lies in isolating the intermediates and their time evolution; either products[5,6] or hole signatures[24,25] are traced, or reaction intermediates without the necessary time resolution[20,21]. In past work, we captured the picosecond population of the surface via the electronic levels of the one-electron water oxidation intermediates, which create states in the middle of the semiconductor bandgap. At the *n*-$SrTiO_3$ surface, we identified the oxyl radical (Ti–O$^\bullet$) that terminates the surface, and the bridge intermediate (T–O$^\bullet$–Ti) parallel to the surface, by a vibration assigned to the oxyl as well as their distinct optical polarization dipoles[26]. As these intermediates were captured following their formation, and under conditions permitting a highly efficient phototrigger (75% charge separation) of Faradaic O_2 evolution[27], we are in a good position to track their decay in the water oxidation cycle.

In this work, by probing the microsecond decay of the mid-gap band with a 400 nm optical probe in reflectance (Supplementary Fig. 1) after phototriggering Faradaic O_2 evolution from the

---

[1]Department of Chemistry, University of California, Berkeley, Berkeley, CA, USA. [2]Chemical Sciences Division, Lawrence Berkeley National Laboratory, Berkeley, CA, USA. [3]Department of Chemistry and Renewable and Sustainable Energy Institute, University of Colorado, Boulder, CO, USA.
*e-mail: tanja.cuk@colorado.edu

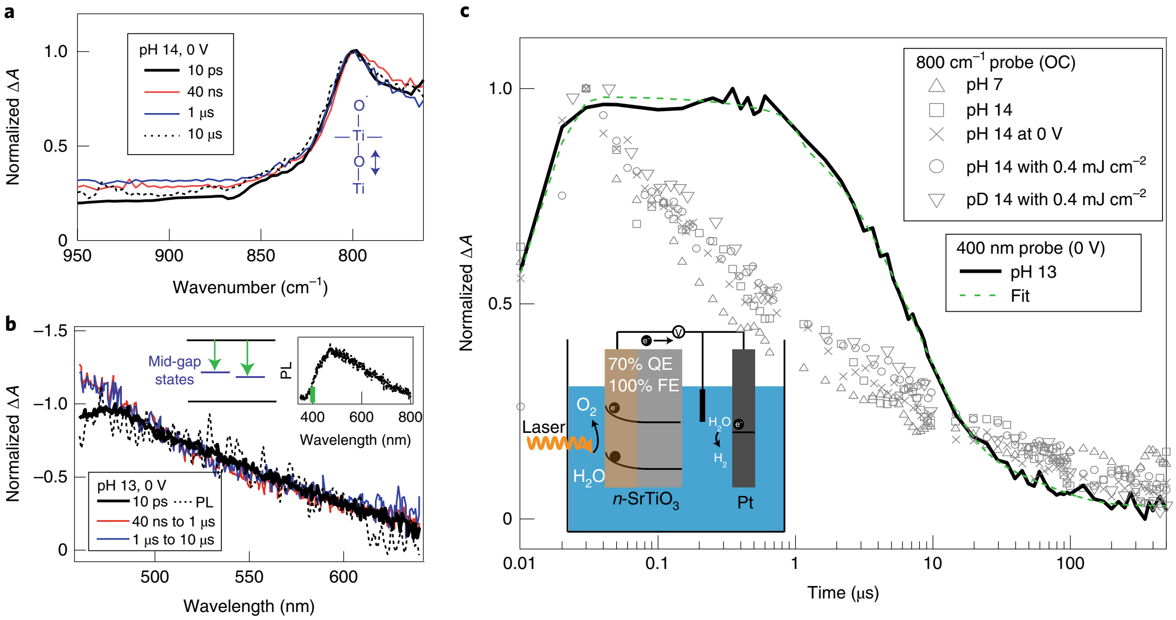

Fig. 1 | Spectra and kinetics of the oxyl and bridge radicals probed through subsurface vibration and the mid-gap electronic levels. a, The time evolution of a representative mid-infrared spectrum (oxyl radical's subsurface vibration) probed in p-polarization at 10 ps (black), 40 ns (red), 1 µs (blue) and 10 µs (black dashed) at pH 14, 0 V versus Ag/AgCl. **b**, The spectrum of the optical transitions of the intermediates measured after excitation at 10 ps (solid black line), 40 ns to 1 µs (time-averaged, red) and 1 µs to 10 µs (time-averaged, blue) compared with photoluminescence spectra (PL) (dashed black) at pH 13, 0 V versus Ag/AgCl. Inset: the photograph shows the photoluminescence spectrum from 350 nm to 800 nm. The green vertical line indicates the optical probe wavelength. The cartoon shows the carriers relaxing from the conduction band to the mid-gap levels, resulting in photoluminescence emission. **c**, The transient kinetics at the peak of the vibration (800 cm^{-1} probe (OC)) for varying experimental conditions (pH, H/D, OC, 0 V versus Ag/AgCl) and on the short wavelength side of the optical spectrum (400 nm, solid line) for pH 13 NaOH solution at 0 V versus Ag/AgCl. The decay of the optical spectrum is different from the infrared spectrum and is well-fitted with a bi-exponential after a pulse limited rise (green dotted line). The inset depicts the photoelectrochemical cell and reaction conditions. OC, open circuit; QE, quantum efficiency; FE, faradaic efficiency.

n-$SrTiO_3$ (Nb 0.1%)/aqueous interface (Supplementary Fig. 2), and by varying the pH, ionic strength, H/D exchange and temperature, we reveal two distinct transition states for the decay of the intermediates. The transition states are defined by two consistent time constants over a large range of reaction conditions, reasonable activation barriers and pre-factors, a kinetic isotope effect (KIE) following H/D exchange on one barrier and a primary kinetic salt effect on both. The primary kinetic salt effect implies multiple site-localized Ti–O$^\bullet$ intermediates in each transition state. We follow the same mid-gap band as that assigned to the oxyl and bridge at ultrafast (picosecond) timescales. The two decay pathways are therefore naturally associated with transition states that re-configure a site previously occupied by either an oxyl or a bridge intermediate. Furthermore, the two pathways occur in parallel, with reaction conditions favouring either the labile (oxyl) or lattice (bridge) intermediate. Recently, such multiple and tuneable routes of O–O bond formation were underscored by the findings of slow and fast sites[21] on the millisecond timescale and two mechanisms separable by the extent of surface excitation[24]. Here, we isolate the activation barriers and character of the transition states, show that they can be described by canonical transition state theory (TST) and demonstrate how to use reaction conditions to favour one pathway over the other.

Electronic and vibrational probes of the reactive surface

Figure 1 depicts the electronic and vibrational spectra of the one-electron intermediates on $SrTiO_3$. The spectra of the oxyl radical's vibration show a subsurface motion of the oxygen beneath the surface/interfacial Ti–O$^\bullet$ (Fig. 1a). The optical spectrum of the oxyl and bridge intermediates results from emissive transitions between the conduction band and their mid-gap electronic states (Fig. 1b). Both of these spectral signatures were defined at ultra-fast timescales immediately following the formation of the intermediates. In particular, the optical spectrum was assigned to holes trapped at oxygen sites—at ultra-fast time-scales, this is the spectrum (decomposed from broadband white light) that arises with the same dynamics with which oxyl and bridge intermediates (probed electronically at 400 nm and vibrationally at 800 cm^{-1} by their characteristic optical and mid-infrared transition dipoles) populate the surface[19,26]. The electronic and vibrational spectra maintain their shape through the observed decay at microsecond timescales, such that they should track the subsequent evolution of the oxyl and bridge intermediates. At low wavelengths, a deviation in the optical spectra is seen at longer times, where spectral distortions could be present at the edge of the sapphire-generated white light spectra and will be investigated with a broader band probe in the future[28]. The optical spectrum tracks the characteristic photoluminescence spectrum from $SrTiO_3$ (ref. [26]), shown in Fig. 1b for the same electrolyte but for an open circuit under steady-state excitation. We also note that both the electronic and vibrational spectra are similarly quenched by methanol, as expected for hole-trapping intermediates (Supplementary Fig. 3).

Figure 1c shows the microsecond decay of the optical (400 nm) and vibrational signatures (800 cm^{-1}) of the intermediates. We find that the heterogeneous kinetics probed by the oxyl's vibration (at 800 cm^{-1}) are insensitive to the reaction conditions for an open (no current flow) or closed (current flow at 0 V versus Ag/AgCl) circuit at pH 7–14, H versus D and surface excitation from 3% to 30%. The closed circuit conditions were taken at pH 14 due to the reactant diffusion limitations in the attenuated total reflection geometry of the mid-infrared evanescent probe[19]. The vibrational transition remains p-polarized throughout, defining a vibration consistently perpendicular to the sample plane (Supplementary Fig. 4). Due to the insensitivity to reaction conditions, the time trace represents oxyl radicals that have yet to react.

Reaction-dependent kinetics of mid-gap electronic levels

We now focus on the well-defined bi-exponential decay that is exhibited by the mid-gap optical transitions, which is highly dependent on the reaction conditions. These will be probed with the narrow band 400 nm pulse at the edge of the photoluminescence spectrum, which explicitly avoids overlapping transitions related to valence band holes (~650 nm)[29,30], Nb dopants[31] and oxygen vacancies[32,33]. The use of 400 nm light also avoids optical transitions that are related to the O–O bond, which could occur at microsecond timescales, but whose electronic states yield molecular orbitals patterns that should not lie in the middle of the gap[34,35]. The 400 nm wavelength cleanly mapped the rise time to populate the surface with the one-electron intermediates onto the vibrational signature (800 cm^{-1}) of the oxyl, probably because it avoids these alternatives. Although highly sensitive to reaction conditions, the bi-exponential decay is well reproduced for different trials and sample batches (Supplementary Figs. 5 and 6). Throughout, the applied potential is kept at 0 V versus Ag/AgCl, at the centre of the potential-independent photocurrent (Supplementary Fig. 2). Although the applied potential does alter the valence band hole potential[29], it does not modify the rates of formation of oxyl and bridge intermediates[26] or, as reported here, the rates of their decay[26] (Supplementary Fig. 7). The activation barrier (E_a) of the reactions we investigate is therefore defined on the reactant side by the electronic potential energy of surface hole traps for Ti–O$^•$ and Ti–O$^•$–Ti intermediates. We report on how the bi-exponential decay rates depend on a range of reaction conditions (pH, H/D exchange and ionic strength); for all of these conditions, the quantum efficiency of charge separation is greater than 70% (Supplementary Figs. 8 and 9). We maintain the surface excitation at 3% (0.04 mJ cm^{-2}), where we have confirmed that separated holes lead to ~100% Faradaic O_2 evolution[27]. The raw data are fit with the equation: $A(t) = A_1 e^{-t/\tau_1} + A_2 e^{-t/\tau_2}$ (Supplementary Note 1). As the exponential fits were carried out from the initial decay, ($A_1 + A_2$) represents the total population of oxyl and bridge intermediates observed at ultra-fast timescales. As the decay evolves, however, each route (A_1 or A_2) is better described by the population of one-electron intermediates, which could include bridge and oxyl forms and different configurations of them, connected to a particular transition state. In the bi-exponential fit, τ_1 and τ_2 represent two parallel routes rather than sequential events in the same cycle. The data were also analysed by several other fitting procedures such as a single exponential, sequential bi-exponential and triple exponential (Supplementary Notes 2–5, Supplementary Figs. 10–13 and Supplementary Tables 1–4). All of these alternative fitting procedures give poorer fits and the bi-exponential fit of two parallel routes is the only one for which τ_1 and τ_2 are constant over a broad pH range. As shown below, the monotonic and physically reasonable parametrization of A_1, τ_1, A_2 and τ_2 over a large range of reaction conditions shows that the data are well described by two parallel and exponentially decaying pathways.

Figure 2 and Supplementary Table 5 show how the bi-exponential decay depends on the pH and H/D isotope exchange at a constant ion density (0.2 M [Na^+]) and 3% surface excitation (Fig. 2a,b shows the raw data and the fits). The relative amplitude ($\frac{A_n}{A_1+A_2}$) (Fig. 3c) of the slower route increases with decreasing pH, which means that the slower route is favoured at lower pH. Over pH 7–13, the two time constants ($\tau_1 \approx 8\,\mu s$ and $\tau_2 \approx 60\,\mu s$) are conserved (Fig. 2d). The systematic trends with pH demonstrate that the decay is not related to a direct charge transfer to spectator anions such as SO_4^{2-} and CO_3^{2-} as the solutions are buffered differently to preserve the ion density (0.2 M [Na^+]) for 7 < pH < 13. We note that the invariance of the decay time constants in this range also implies that there is no direct charge transfer to the hydroxide ions in solution (Fig. 3). Above pH 13, both time constants exhibit a marked decrease, reflecting a faster mechanism. At this stage, we do not differentiate between an ion density and pH effect in highly basic conditions as high pH alone could speed up the reaction in accordance with a number of previous electrochemical investigations of O_2 evolution[36–38]. Finally, an H/D KIE demarcates a separate mechanism for the slower route. With deuterated water, the slower decay (Fig. 2b) reflects a constant H/D KIE of ~1.75 on τ_2 (Fig. 2d). Although a few H/D KIEs have been reported for water oxidation at electrode surfaces, they are based on time-resolved photocurrent[37] or steady-state product evolution[38] rather than the decay of an intermediate and they do not exhibit systematics with the reaction conditions as seen here.

Figure 3 shows how the bi-exponential decay depends on ionic strength and surface excitation at pH 7. At constant surface excitation (7×10^{13} cm^{-2} or 3% of oxygen sites), ion density greatly affects which route is favoured (Fig. 3a,b), with the slower route dominating at 0.02 M [Na^+] and with equal contributions of both by 1 M [Na^+]. Importantly, iondensity does not modify the overall signal amplitude: the faster route's contribution to the decay increases directly at the expense of the slower route, further identifying two parallel pathways (Fig. 3b). An unchanged signal amplitude over a molarity range from 0 to 4 M [Na^+] also means that although ion density can change the protonation of the surface[39], it is not substantial enough to modify the initial conditions giving rise to the electronic levels of A_1+A_2. We note that bulk pH, by contrast, does change the initial optical cross-section considerably, leading to the relative magnitudes $\frac{A_n}{A_1+A_2}$ reported. Therefore, a similar surface population of localized oxyl and bridge intermediates, created at picosecond timescales and determined by a given pH, exhibits a nanosecond branching into the two populations (A_1 and A_2). Increasing the ion density also decreases τ_1 and τ_2 and the effect saturates at 1 M (Fig. 3c).

As the ion density clearly tunes the time constants and populations, screening of the electrode surface by the electrolyte modulates the two reaction pathways. To quantitatively account for such screening, the ion density is plotted as the cation surface density of a sphere of the bulk electrolyte. For the electrolyte Na_2SO_4, the cation surface density ([Na^+]$_s$) is equivalent to the negative charge contained in the anion (SO_4^{2-}) surface density. Plotted this way, 1 M translates to 7×10^{13} cm^{-2} [Na^+]$_s$, which means that the ion density effects saturate approximately when the anion charge density equals the surface hole excitation (dotted lines in Fig. 3b,c). If the surface excitation decreases by half, the saturation point decreases accordingly (black versus red in Fig. 3b,c). As the ion density was modulated at a constant and neutral pH, the anions (SO_4^{2-}) screen the population of one-electron intermediates at oxygen sites. These results implicate screening, in the planar sense, to the bifurcation of the population between two reaction pathways.

Rate constants in TST

Two decay rates systematically tuned by pH, ion density and H/D exchange demonstrate reaction-dependent activation barriers. Transition state theory explicitly connects rate constants to a transition state by modulating reaction conditions that affect only the activation barrier, but not the population of the reacting species[40]. In doing so, the theory allows a connection to the transition state to be made without postulating a specific mechanism. We explicitly explore temperature and then the ionic strength in this context. In TST, reaction rates (κ_n) are equal to $Qe^{-E_a/kT}$, where E_a is the activation energy, Q is the reaction pre-factor, T is the temperature and k is Boltzmann's constant. Figure 3d shows the decay dynamics for different temperatures at pH 11 with 0.2 M sodium ion concentration at 0 V versus Ag/AgCl. A pH 11 solution is chosen because at this pH the τ_1 and τ_2 decay pathways contribute fairly equally

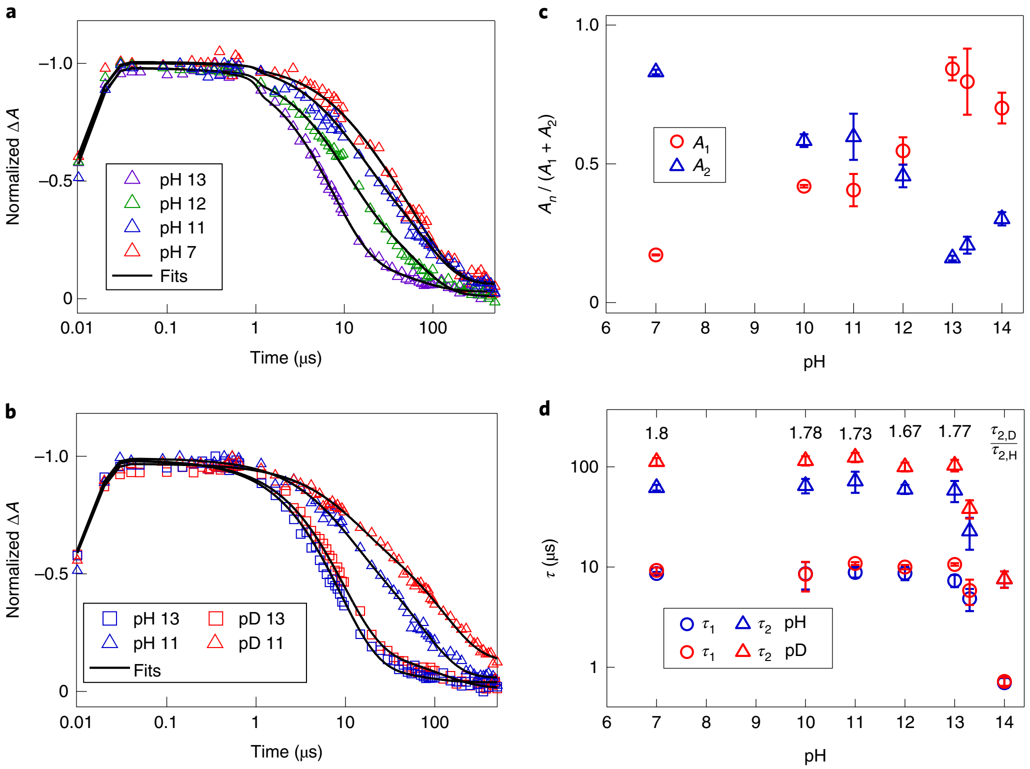

Fig. 2 | The pH dependence and H/D KIE at the same ion density (0.2 M [Na$^+$]). **a**,**b**, Normalized transient kinetics at 0 V versus Ag/AgCl with a 400 nm probe fit with bi-exponential decays: for different pH (**a**) and for pH/pD 11 and pH/pD 13 (**b**). **c**, The pH-dependent relative amplitudes [$A_n/(A_1 + A_2)$] of the decay. **d**, The pH-dependent time constants of the two decay routes (τ_1, τ_2) in both normal and deuterated water. Uncertainties in **c** and **d** come from the standard deviation of the fitting parameters. The H/D KIE ~1.75 of the slower decay route (τ_2) is plotted for pH 7–13 on the top axis as deuterated water does not change (within 6.5%) the amplitudes (A_1, A_2) associated with each decay route. To maintain a 0.2 M [Na$^+$] of the electrolyte for 7 < pH < 13, different buffers were used (see Methods for details).

through A_1 and A_2, making it relatively easy to see the effect of temperature on both decay pathways. The dynamics were reproducible for 295 K (room temperature) < T < 330 K as indicated by the 328 K curve (trial 2 in Fig. 3d). The fitted reaction rates κ_n ($1/\tau_n$) are shown in Fig. 3e. With increasing temperature, both κ_1 and κ_2 increase. More importantly, κ_1 and κ_2 are logarithmically (ln) dependent on $1/T$. The processes defining κ_1 are different than κ_2, with κ_1 much larger than κ_2 for all temperature points on the logarithmic plot. In TST, the difference either originates from Q or E_a. In a free linear fit of the data (which gives us the best R^2 (0.95)), the activation barriers are 0.38 ± 0.06 eV and 0.5 ± 0.08 eV and the pre-factors are 0.4 ± 0.1 THz and 5 ± 0.1 THz respectively for κ_1 and κ_2. In this free fit, the rate difference arises from the lower activation barrier for κ_1. As the activation barriers overlap within the error, we also performed the linear fit by fixing the activation barrier to the region of overlap (0.42–0.44 eV). With a fixed activation barrier for both routes, A instead differentiates the faster route from the slower route, with values of 4.9 ± 0.1 THz and 4.3 ± 0.1 THz, respectively, albeit with lower R^2 values (Supplementary Figs. 14 and 15). The analysis clearly separates the two processes but cannot fully define the origin of the rate difference in the Arrhenius model. However, in all cases the slopes define E_a values of ~0.4–0.5 eV, consistent with that expected for O–O bond formation events by DFT calculations[41,42]. Furthermore, the pre-factors are within 0.4–5 THz, which is the relevant range for TST that anticipates $\frac{kT}{h} \approx 6$ THz for events where each relevant vibration transmits a reactant across the barrier (h is Planck's constant).

If the reactants that create the transition state involve ions or trapped charge, the solution ionic strength can modulate the activation barrier by screening the charge distribution in the transition state. For screening to affect the barrier, at least two reactants must be involved. The Bronsted–Bjerrum equation[43,44] defines this primary kinetic salt effect and is given for a bimolecular reaction by:

$$\log \kappa = \log \kappa_0 + 1.02\, Z_A Z_B I^{1/2} \qquad (1)$$

where κ is the measured rate, κ_0 is the rate in the absence of a salt, Z_A and Z_B are the charges associated with reactants A and B, and I is the ionic strength of the solution; $I = 0.5 \sum C_i Z_i^2$, where C_i and Z_i are the concentration of the ion solution and the charge on each, respectively. Figure 3f recasts the τ_1, τ_2 dependence of [Na$^+$]$_s$ on I, revealing a square-root relationship between the reaction rate and I, and a positive $Z_A Z_B$. This positive $Z_A Z_B$ means that two reactants of the same type of charge are associated with the transition state, such that counter ions screen them from each other and increase the rate through the barrier. Therefore, the Bronsted–Bjerrum equation confirms and further explains the above interpretation: solution anions screen interactions between two or more one-electron intermediates. Moreover, it connects this screening to the transition state. Using the bimolecular description as an example, the screening is stronger for the κ_1 ($Z_A Z_B = 0.51 \pm 0.14$, $\chi^2 = 0.15$) than the κ_2 ($Z_A Z_B = 0.13 \pm 0.03$, $\chi^2 = 0.04$) transition state; $Z_A Z_B$ is less than one in both, which means that the charge on the oxygen sites is less than a full valence band hole, as anticipated for charge trapping associated with proton transfers (for example, Ti–OH to Ti–O$^\bullet$).

Discussion

The cumulative observations demonstrate the TST dynamics of two local water oxidation transition states at an electrode surface, which

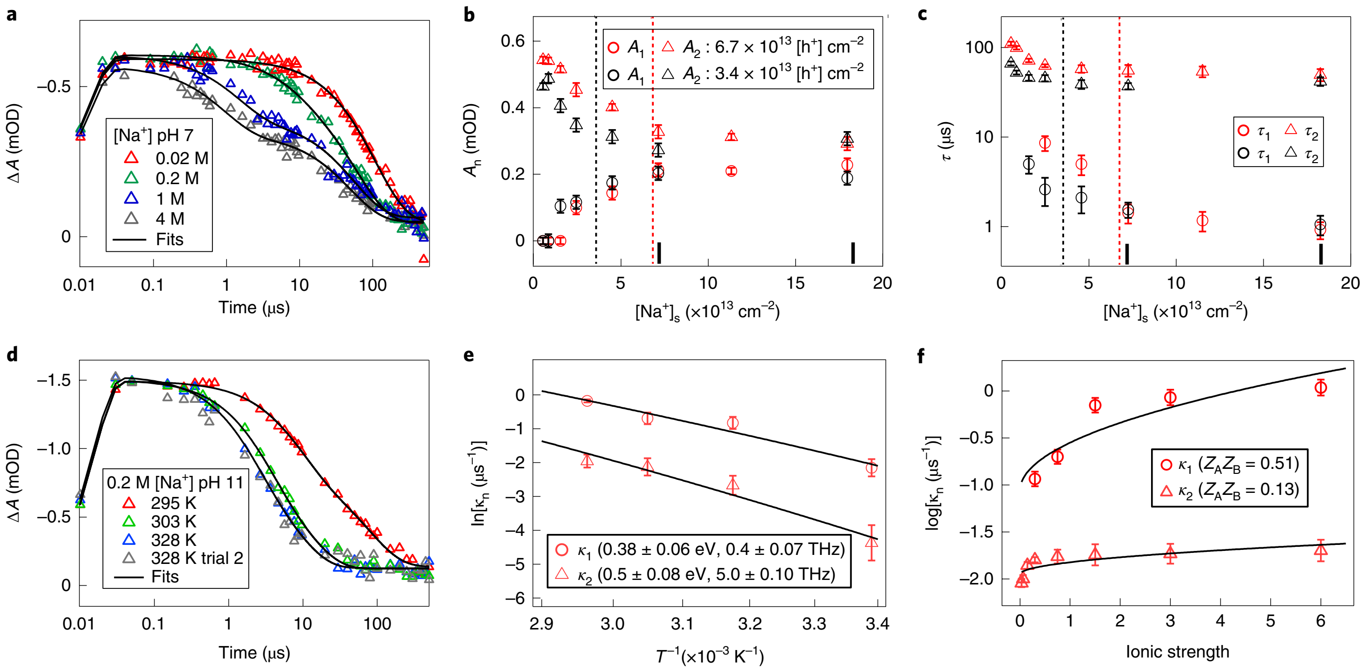

Fig. 3 | Ionic strength and temperature dependence at constant pH. **a**, Transient kinetics measured at pH 7 for increasing density of [Na$^+$] (supplied with Na_2SO_4) and fitted with bi-exponential decays. **b**, The amplitudes of the two decay routes (A_1, A_2) plotted against $[Na^+]_s$ or equivalently the total negative surface charge coming from SO_4^{2-} (the *x*-axis bars indicate 1 M and 4 M [Na$^+$]). The amplitudes are shown for two surface hole excitations ([h$^+$] cm^{-2}) (see legend). **c**, The lifetime of the two decay routes (τ_1, τ_2) plotted against $[Na^+]_s$ for the two surface hole excitations (see legend in **b**). The vertical dotted lines in **b** and **c** indicate where $[Na^+]_s$ equals the surface hole density. The uncertainties in **b** and **c** come from the standard deviation associated with the fitting parameters. **d**, The selected transient kinetics for the 0.1% Nb-doped $SrTiO_3$ in pH 11 solution with 0.2 M [Na$^+$] at different temperatures with fits; the reproducible faster decay dynamics that is observed for increasing temperature are as indicated by trial 2 at 328 K. **e**, The logarithmic (ln) dependence of decay rates (κ_1 (μs^{-1}) defined as ($1/\tau_1$), and κ_2 (μs^{-1}) defined as ($1/\tau_2$)) on $1/T$. The slopes and intercepts of the fits (black lines) to the data (red symbols) reveal the energies and pre-factors, respectively. The uncertainties in the rate constants come from standard deviations of at least six different trials at the same temperature. The uncertainty of the activation barriers and pre-factors came from least-square linear fitting. **f**, The logarithmic (log) dependence of the decay rates (κ_1, κ_2) on the square root of *I*, shown through the fits (black line) to the data (red symbols). The steepness of the dependence is defined by the charge on the reactants (Z_AZ_B) in the transition state.

isolates a reaction barrier from the four expected in the cycle. The transition states are inherently local because they are defined by two (rather than many) distinct reaction rates, one of which exhibits a unique H/D KIE, and both of which reflect screened transition states through the primary kinetic salt effect. That both routes are relevant for the water oxidation cycle is understood through the pathway dependence on reaction conditions, in the context of the experimental set-up in which the initial charge-trapping intermediates achieve Faradaic O_2 evolution. The reaction conditions monotonically tune the pathways such that either can dominantly contribute to the decay associated with O_2 evolution. This is especially clear with the dependence on ionic strength, which bifurcates the initial population into the two pathways.

We next consider the assignment of the two competing transition states, given that one should relate to the decay of an oxyl site and the other to a bridge site (Fig. 4). The pathway (A_1,A_2) and rate ($\kappa_1(1/\tau_1)$, $\kappa_2(1/\tau_2)$) dependence on pH, ionic strength and KIE assigns the faster κ_1 to the oxyl as, first, higher pH favours a dissociated Ti–O$^-$ terminated surface and so a higher relative population of oxyls. Second, screening should affect primarily the labile oxyl radical. Third, at very low ionic strengths, oxyl radicals are not screened and therefore the route of bond formation through them is not supported ($A_1 \approx 0$), and, finally, the KIE is negligible. All four observations are relevant to the commonly cited biradical recombination mechanism of O–O bond formation from two neighbouring oxyl radicals[18,45]. Therefore, direct coupling of adjacent Ti–O (oxyl) to form a TiOOTi peroxo species is a likely mechanism (Fig. 4). Further, this mechanism requires two localized intermediates in the transition state, which is reflected in the primary kinetic salt effect. Although observed for both pathways, the Bronsted–Bjerrjum equation has a larger Z_AZ_B for the faster κ_1 pathway.

We assign the slower κ_2 pathway to a reaction through the lattice (bridge) intermediate. The distinct H/D KIE points to the participation of a water or hydroxyl molecule in the formation of the transition state. We speculate that a surface TiOOH (peroxo) is formed as a result of nucleophilic attack of neighbouring oxyl and lattice intermediates by a water molecule (see Fig. 4)[45–48]. The remaining proton from the water molecule attaches itself to a hydroxide ion, which leads to the formation of an additional water molecule, fitting with the observation that this pathway is favoured at lower pH. Considering that the nucleophilic attack mechanism involves breaking the O–H bond, it could relate to the observed KIE. However, the value of ~1.75 KIE is lower than expected for a pure O–H breaking event, suggesting that it is masked by screening, either by counter ions in the electrolyte or the involvement of hydroxide ions in the transition state. The lower Z_AZ_B on the primary kinetic salt effect also suggests that the screening between the intermediates in the transition state is more complex. It is interesting that a similarly low H/D KIE was measured for O_2 evolution from the water oxidation complex in photosystem II (refs. [13,18]). Both of the above pathways result in peroxo (O–O) formation for which only two hole transfers are required. However, we emphasize that the data do not elucidate whether the species formed is a peroxo or a superoxo (for example, O–O•), which would require three hole transfers. The primary

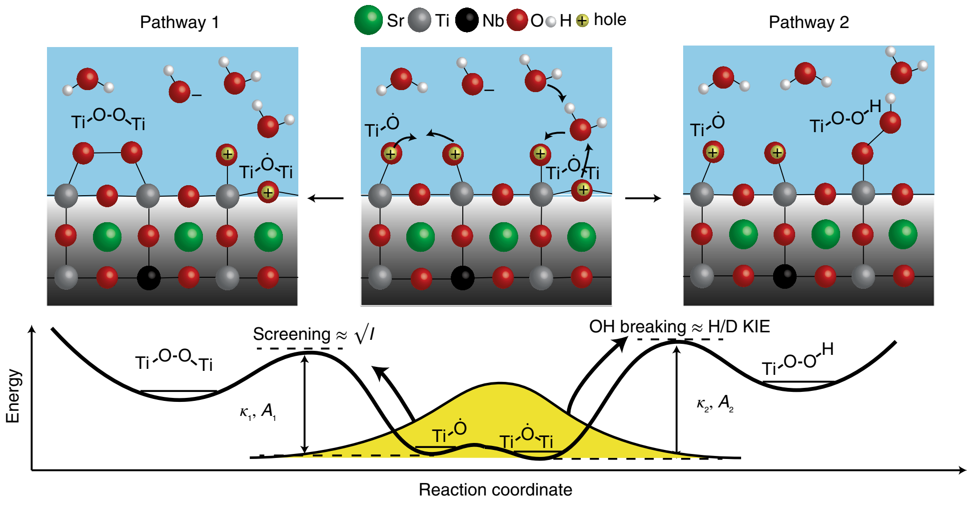

Fig. 4 | Two competing reaction pathways. A cartoon and free-energy description of the two reaction pathways described experimentally are shown, with the distributed configurations of the principal intermediates represented as the yellow Gaussian distribution. The cartoon proposes two reaction pathways for O–O bond formation. A likely result of the faster pathway 1 is a surface TiOOTi species by biradical recombination, whereas a likely result of the slower pathway 2 is a surface TiOOH species by nucleophilic attack.

kinetic salt effect only defines two or more localized hole-transfer intermediates to be present in the transition state. We note that neither pathway exhibits a measurable $^{16}O/^{18}O$ KIE (Supplementary Fig. 16), which is consistent with mechanisms that do not involve breaking an O–O bond.

We now turn to how these TST dynamics were revealed at an electrode surface. These dynamics should reflect the full range of reactant configurations involved: in the reactant quasi-equilibrium description of TST, the transition state is in a quasi-equilibrium with the entire reactant population, which includes that site undergoing the transformation and how it interacts with neighbouring sites. The reactant population therefore includes site-localized bridge and oxyl intermediates (from which an O–O bond might form) and their time-dependent configurations. Molecular dynamics simulations identify that diffusive surface-hopping should exist on titania surfaces: local exchange of a hole at neighbouring oxygen sites turns a bridge intermediate into an oxyl, and vice versa, on the picosecond timescale[23]. Such diffusive hopping should lead to many different configurations of oxyl and bridge intermediates. This is especially the case for 3% surface excitation, which separates hole-trapping intermediates from each other by at most around two unit cells, such that even short-range hopping could lead to a large distribution. In this context, a broadband (~1 eV) optical probe of TST—which averages over all of the possible intermediate configurations through their mid-gap electronic levels—can detect the TST dynamics, whereas the infrared probe of the normal modes of a specific site-localized intermediate does not. Indeed, the results advance that transition states exist separately from a specific reactant, as reaction conditions branch the populations into two separate population pathways, implying that the decay of any one site depends highly on the configuration of its neighbouring ones. Invistigating this dichtomy could be a very promising avenue for future work, perhaps through the suface hopping of the intermediates, in which the surface as a whole rather than a particular surface site leads to catalytic events. The distributed reactant configurations that can reach either transition states are depicted in yellow in Fig. 4.

In summary, we use canonical TST to demonstrate competing pathways by which the charge-trapping intermediates (the oxyl and bridge) of the water oxidation reaction on $SrTiO_3$ surfaces decay towards the next step in the reaction. The competing pathways reflect what has often been considered important for electrode surfaces: the multitude of sites allows for multiple mechanisms. One of the challenges was to identify the transition states clearly enough to understand how to tune between disparate mechanisms. By isolating the decay of the intermediates, we demonstrate how to use reaction conditions (pH, ionic strength) to select between two competing transition states. The ionic strength is especially interesting, as it can branch a similar initial population of the oxyl and bridge intermediates fully towards the slower route or create equal populations through the fast and slow routes.

Methods

Samples. Single crystals of 0.08% Nb-doped $SrTiO_3$ by weight (henceforth, 0.08% is approximated to 0.1%) with a crystallographic orientation of (100) were obtained from MTI Corp. The crystals were 0.5 mm thick with polished frontsides (Ra < 5 Å) and unpolished backsides; all spectroscopic measurements were performed on the polished frontsides. All spectroelectrochemical measurements were performed in a Teflon electrochemical cell with CaF_2 optical windows (3 mm thick). The electrolyte was in contact with the atmosphere during measurements. The potential of the n-$SrTiO_3$ photoelectrode—with respect to the Ag/AgCl (3 M KCl) reference electrode (MF-2052, Basi)—was controlled by a CHI650E Potentiostat (CH Instruments). A Pt wire served as the counter electrode. Ohmic contact between the unpolished n-$SrTiO_3$ backside and the copper wire was established using a gallium–indium eutectic (Sigma Aldrich). For the transient reflectance experiments, an insulating lacquer covered all of the surfaces except the polished frontside of the crystal. The exposed front surface areas of the 0.1% and Nb-doped samples were 25 mm^2.

Transient experiments. For the transient optical experiments, the pump beam was derived from a Nd:YAG laser system that produced pulses with a centre wavelength of 1,064 nm and ~40 ns temporal width at a 1 kHz repetition rate. All of the output was directed into a Fourth harmonic generation set-up to generate 266 nm light as a pump. The probe beam was derived from a regeneratively amplified Ti:sapphire laser system (Coherent Legend, Coherent, Inc.) that produced pulses with a centre wavelength of 800 nm and ~150 fs temporal width at a 1 kHz repetition rate. Part of the 800 nm beam was frequency doubled to generate 400 nm light or focused into a sapphire crystal to generate white light as a probe (the detailed sample configuration can be seen in Supplementary Fig. 1). The polarization of the 400 nm probe beam was controlled by changing the 800 nm polarization using a half-wave plate and a linear polarizer. The pump beam was incident normal to the sample surface. After the sample, the reflected probe beam was focused into an optical fibre, which was coupled to a CMOS array spectrometer (CAM-VIS-3, Ultra-fast Systems, LLC). In all of the experiments, the pump beam was modulated by a mechanical chopper (3501, Newport, Inc.) at a frequency of 500 Hz. The detector output was interfaced with a personal computer, which provided automated control over an electronic delay generator (DG645, Stanford Research Systems). The typical incident pump fluence was about 0.05 mJ cm^{-2} at 266 nm, corresponding to 6.7×10^{13} photons per cm^2. For a typical n-$SrTiO_3$ (100) surface with a lattice constant of 3.905 Å, the number of oxygen atoms is close to 1.97×10^{15} atoms per cm^2. Therefore, for a 0.05 mJ cm^{-2} fluence at >70% quantum efficiency charge separation, the surface excitation is close to 3.4% (counting oxygen atoms). The excitation beam spot size was ~500 μm (full-width at half maximum).

Transient spectroscopy measurements were conducted in an electrochemical cell in reflection geometry. Six scans were performed and averaged to extract a single kinetic trace. Each scan was performed on a fresh sample spot and took less than 90 s to avoid deterioration of the signal by sample surface roughening[29]. The current observed following light excitation by 266 nm laser pulses during the ~90 s excitation was stable, and represented >70% charge separation efficiency. These conditions did not change (within the fluence error of ±0.005 mJ cm^{-2}) for a Cu counter electrode compared to the usual Pt counter electrode, showing that the dissolution/redeposition of Pt does not interfere with the results (Supplementary Fig. 17). The temperature of the electrochemical cell was controlled by a heating gun. The solution temperature was monitored with a thermal couple before and after the experiment to ensure that the temperature was stable. In general, the temperature was stable within ±3 K°. For the pH and pD experiments, the solution was buffered with Na_2SO_4, $NaHCO_3$, Na_2CO_3 and NaOH; the pH 7 solution was buffered with Na_2SO_4; the pH 12 and 13 solutions were buffered with Na_2SO_4 and NaOH; and the pH 10 and 11 solutions were buffered with $NaHCO_3$, Na_2CO_3 and Na_2SO_4. The pump beam for the transient infrared measurement was derived in the same way as the optical measurement. Other procedures were kept the same with previous infrared measurements[19].

Data availability

The representative data and all of the analysis from the extended dataset that support the findings of this paper are available in the paper and the Supplementary Information. The extended dataset that supports the findings in this paper is available from the corresponding author on reasonable request.

Received: 2 March 2019; Accepted: 28 June 2019;

References

1. Hwang, J. et al. Perovskites in catalysis and electrocatalysis. *Science* **358**, 751–756 (2017).
2. Seh, Z. W. et al. Combining theory and experiment in electrocatalysis: insights into materials design. *Science* **355**, eaad4998 (2017).
3. Markovic, N. M. Electrocatalysis: interfacing electrochemistry. *Nat. Mater.* **12**, 101–102 (2013).
4. Bockris, J. O. M. & Otagawa, T. The electrocatalysis of oxygen evolution on perovskites. *J. Electrochem. Soc.* **131**, 290–302 (1984).
5. Surendranath, Y., Kanan, M. W. & Nocera, D. G. Mechanistic studies of the oxygen evolution reaction by a cobalt-phosphate catalyst at neutral pH. *J. Am. Chem. Soc.* **132**, 16501–16509 (2010).
6. Yeo, B. S. & Bell, A. T. Enhanced activity of gold-supported cobalt oxide for the electrochemical evolution of oxygen. *J. Am. Chem. Soc.* **133**, 5587–5593 (2011).
7. Seitz, L. et al. A highly active and stable $IrO_x/SrIrO_3$ catalyst for the oxygen evolution reaction. *Science* **353**, 1011–1014 (2016).
8. Li, Y. F., Liu, Z. P., Liui, L. & Gao, W. Mechanism and activity of photocatalytic oxygen evolution on titania anatase in aqueous surroundings. *J. Am. Chem. Soc.* **132**, 13008–13015 (2010).
9. Zhang, M. & Frei, H. Towards a molecular level understanding of the multi-electron catalysis of water oxidation on metal oxide surfaces. *Catal. Lett.* **145**, 420–435 (2014).
10. Rossmeisl, J., Qu, Z. W., Zhu, H., Kroes, G. J. & Nørskov, J. K. Electrolysis of water on oxide surfaces. *J. Electroanal. Chem.* **607**, 83–89 (2007).
11. Nørskov, J. K. et al. Universality in heterogeneous catalysis. *J. Catal.* **209**, 275–278 (2002).
12. Pijpers, J. J. H., Winkler, M. T., Surendranath, Y., Buonassisi, T. & Nocera, D. G. Light-induced water oxidation at silicon electrodes functionalized with a cobalt oxygen-evolving catalyst. *Proc. Natl Acad. Sci. USA* **108**, 10056–10061 (2011).
13. Blakemore, J. D., Crabtree, R. H. & Brudvig, G. W. Molecular catalysts for water oxidation. *Chem. Rev.* **115**, 12974–13005 (2015).
14. Yano, J. & Yachandra, V. K. Where water is oxidized to dioxygen: structure of the photosynthetic Mn_4Ca cluster from X-ray spectroscopy. *Inorg. Chem.* **47**, 1711–1726 (2008).
15. Askerka, M., Brudvig, G. W. & Batista, V. S. The O_2-evolving complex of photosystem II: recent insights from quantum mechanics/molecular mechanics (QM/MM), extended X-ray absorption fine structure (EXAFS), and femtosecond X-ray crystallography data. *Acc. Chem. Res.* **50**, 41–48 (2017).
16. Noguchi, T. Light-induced FTIR difference spectroscopy as a powerful tool toward understanding the molecular mechanism of photosynthetic oxygen evolution. *Photo. Res.* **91**, 59–69 (2007).
17. Zaharieva, I., Wichmann, J. M. & Dau, H. Thermodynamic limitations of photosynthetic water oxidation at high proton concentrations. *J. Bio. Chem.* **286**, 18222–18228 (2011).
18. Zaharieva, I., Dau, H. & Haumann, M. Sequential and coupled proton and electron transfer events in the S2 → S3 transition of photosynthetic water oxidation revealed by time-resolved X-ray absorption spectroscopy. *Biochemistry* **55**, 6996–7004 (2016).
19. Herlihy, D. M. et al. Detecting the oxyl radical of photocatalytic water oxidation at an *n*-$SrTiO_3$/aqueous interface through its subsurface vibration. *Nat. Chem.* **8**, 549–555 (2016).
20. Zandi, O. & Hamann, T. W. Determination of photoelectrochemical water oxidation intermediates on haematite electrode surfaces using operando infrared spectroscopy. *Nat. Chem.* **8**, 778–783 (2016).
21. Zhang, M., de Respinis, M. & Frei, H. Time-resolved observations of water oxidation intermediates on a cobalt oxide nanoparticle catalyst. *Nat. Chem.* **6**, 362–367 (2014).
22. Pham, H. H., Cheng, M.-J., Frei, H. & Wang, L.-W. Surface proton hopping and fast-kinetics pathway of water oxidation on Co_3O_4 (001) surface. *ACS Catal.* **6**, 5610–5617 (2016).
23. Cheng, J., Vandevondele, J. & Sprik, M. Identifying trapped electronic holes at the aqueous TiO_2 interface. *J. Phys. Chem. C* **118**, 5437–5444 (2014).
24. Formal, F. L. et al. Rate law analysis of water oxidation on a hematite surface. *J. Am. Chem. Soc.* **137**, 6629–6637 (2015).
25. Pendlebury, S. R. et al. Ultrafast charge carrier recombination and trapping in hematite photoanodes under applied bias. *J. Am. Chem. Soc.* **136**, 9854–9857 (2014).
26. Chen, X. et al. The formation time of Ti–O• and Ti–O•–Ti Radicals at the *n*-$SrTiO_3$/aqueous interface during photocatalytic water oxidation. *J. Am. Chem. Soc.* **139**, 1830–1841 (2017).
27. Aschaffenburg, D. J., Chen, X. & Cuk, T. Faradaic oxygen evolution from $SrTiO_3$ under nano- and femto-second pulsed light excitation. *Chem. Commun.* **53**, 7254–7257 (2017).
28. Likforman, J. P., Alexandrou, A., Joffre, M. & Fejer, M. Femtosecond white-light continuum generation in a Ti:sapphire oscillator. in *Advanced Solid State Lasers* (eds. Bosenberg, W & Fejer, M.) Vol. 19, TS5 (Optical Society of America, 1998).
29. Waegele, M. M., Chen, X., Herlihy, D. M. & Cuk, T. How surface potential determines the kinetics of the first hole transfer of photocatalytic water oxidation. *J. Am. Chem. Soc.* **136**, 10632–10639 (2014).
30. Yamada, Y., Yasuda, H., Tayagaki, T. & Kanemitsu, Y. Photocarrier recombination dynamics in highly excited $SrTiO_3$ studied by transient absorption and photoluminescence spectroscopy. *Appl. Phys. Lett.* **95**, 121112 (2009).
31. Higuchi, T. et al. Electronic structure in the band gap of lightly doped $SrTiO_3$ by high-resolution X-ray absorption spectroscopy. *Phys. Rev. B* **61**, 12860–12863 (2000).
32. Mitra, C., Lin, C., Robertson, J. & Demkov, A. A. Electronic structure of oxygen vacancies in $SrTiO_3$ and $LaAlO_3$. *Phys. Rev. B* **86**, 155105 (2012).
33. Janotti, A., Varley, J. B., Choi, M. & Van de Walle, C. G. Vacancies and small polarons in $SrTiO_3$. *Phys. Rev. B* **90**, 085202 (2014).
34. Chen, H. & Umezawa, N. Hole localization, migration, and the formation of peroxide anion in perovskite $SrTiO_3$. *Phys. Rev. B* **90**, 035202 (2014).
35. Guhl, H., Miller, W. & Reuter, K. Oxygen adatoms at $SrTiO_3$(001): a density-functional theory study. *Surf. Sci.* **604**, 372–376 (2010).
36. Kafizas, A. et al. Water oxidation kinetics of accumulated holes on the surface of a TiO_2 photoanode: a rate law analysis. *ACS Catal.* **7**, 4896–4903 (2017).
37. Norton, A. P., Bernasek, S. L. & Bocarsly, A. B. Mechanistic aspects of the photooxidation of water at the n-titania/aqueous interface: optically induced transients as a kinetic probe. *J. Phys. Chem.* **92**, 6009–6016 (1988).
38. Zhang, Y. et al. Pivotal role and regulation of proton transfer in water oxidation on hematite photoanodes. *J. Am. Chem. Soc.* **138**, 2705–2711 (2016).
39. De Stefano, C., Foti, C., Giuffrè, O. & Sammartano, S. Dependence on ionic strength of protonation enthalpies of polycarboxylate anions in NaCl aqueous solution. *J. Chem. Eng. Data* **46**, 1417–1424 (2001).
40. Eyring, H. The activated complex in chemical reactions. *J. Chem. Phys.* **3**, 107–115 (1935).
41. Lundberg, M., Blomberg, M. R. & Siegbahn, P. E. Oxyl radical required for O–O bond formation in synthetic Mn-catalyst. *Inorg. Chem.* **43**, 264–274 (2004).
42. Li, X. & Siegbahn, P. E. Alternative mechanisms for O_2 release and O–O bond formation in the oxygen evolving complex of photosystem II. *Phys. Chem. Chem. Phys.* **17**, 12168–12174 (2015).
43. Bronsted, J. N. Theory of the chemical reaction rate. *Z. Phys. Chem.* **102**, 169–207 (1922).
44. Steinfeld, J. I., Francisco, J. S. & Hase, W. L. *Chemical Kinetics and Dynamics* 2nd edn (Prentice Hall, 1998).

45. Li, F. et al. Immobilizing Ru(bda) catalyst on a photoanode via electrochemical polymerization for light-driven water splitting. *ACS Catal.* **5**, 3786–3790 (2015).
46. Oloo, W. N., Fielding, A. J. & Que, L. Rate-determining water-assisted O–O Bond Cleavage of an Fe^{III}–OOH intermediate in a bio-inspired nonheme iron-catalyzed oxidation. *J. Am. Chem. Soc.* **135**, 6438–6441 (2013).
47. Saavedra, J., Doan, H. A., Pursell, C. J., Grabow, L. C. & Chandler, B. D. The critical role of water at the gold-titania interface in catalytic CO oxidation. *Science* **345**, 1599–1602 (2014).
48. Wijeratne, G. B., Day, V. W. & Jackson, T. A. O–H bond oxidation by a monomeric Mn^{III}–OMe complex. *Dalton Trans.* **44**, 3295–3306 (2015).p

Acknowledgements

The experimental work was supported by the Director, Office of Science, Office of Basic Energy Sciences, and by the Division of Chemical Sciences, Geosciences and Biosciences of the US Department of Energy at LBNL under contract no. DE-AC02–05CH11231. We thank H. Frei and J. Eaves for fruitful discussions.

Author contributions

T.C. and X.C. conceived the project and T.C. wrote the manuscript with input from all authors. X.C and D.J.A constructed the transient set-up, collected transient data and prepared samples. X.C and T.C. analysed the transient data.

Competing interests

The authors declare no competing interests.

Additional information

Supplementary information is available for this paper at https://doi.org/10.1038/s41929-019-0332-5.

Reprints and permissions information is available at www.nature.com/reprints.

Correspondence and requests for materials should be addressed to T.C.